# Galling categories investigations in stainless steels

T. Lesage, Salima Bouvier, A. Oudriss, Y. Chen, Marion Risbet, P.-E. Mazeran

# Galling categories investigations in stainless steels

T. Lesage[1,*], S. Bouvier[1], A. Oudriss[2], Y. Chen[3], M. Risbet[1], P-E. Mazeran[1]

[1] Sorbonne University, UTC, CNRS, FRE 2012 Roberval, France

[2] LaSIE, CNRS UMR 7356, Université de La Rochelle, La Rochelle, France

[3] CETIM, Pôle matériaux métalliques et surfaces, Senlis, France

Corresponding author: thibault.lesage@railenium.eu – 180 Rue Joseph-Louis Lagrange, 59540 Valenciennes, France

## *Abstract*

This paper focuses on the galling mechanisms occurring in stainless steels and aims to provide a better comprehension of the effects of microstructure on galling resistance. Five stainless steels are studied in this paper, namely Nitronic60, AISI660, 316L, 316LN (austenitic stainless steels) and Uranus45N (duplex austenite-ferrite). Both surface topography and in-depth microstructure are characterized in order to determine the consequences of galling apparition. Experimental investigations at macroscopic and microscopic scales show that galling can occur following several mechanisms. Galling leads to either adhesive wear spots randomly distributed on the surface (tolerant galling), adhesive wear initiated on the periphery of the pin (moderate galling) or abrasive wear and smearing (severe galling). Depending on these categories, the galling threshold and severity are highly variable. Studying these specific mechanisms can help us predict and eventually increase galling resistance for a given material couple. Thus, several microstructural investigations have been performed in order to discuss about the possible origins of these galling categories.

**Keywords: Galling mechanisms, surface topography, microstructure, stainless steels**

# 1. Introduction

Galling is a severe case of adhesive wear, defined by the ASTM committee G02 on wear and erosion in Standard G40 [1] as "a form of surface damage arising between sliding solids, distinguished by macroscopic, usually localized, roughening and creation of protrusions above the original surface". Galling goes with the apparition of undesirable surface modifications, leading to the deterioration of the materials in contact [2]. Galling is problematic for a wide range of industrial applications, e.g. medical instruments, sheet metal forming, nuclear plants [3]. In most of these industries, stainless steels are widely used due to their relative ease of manufacture, high strength, stiffness and excellent corrosion resistance. However, stainless steels are likely to develop galling [4,5], making galling resistance one of the key parameters in determining tool lifetime in such industries [6]. Even though the use of lubricants can easily lower the tendency to galling [7], lubrication could be undesirable *e.g.* in food-processing or pharmaceutical industries, which explains the increasing interest in dry sliding conditions [8]. As a consequence, numerous studies focus on increasing galling resistance [9–11] of different materials couples. Several factors are already known to increase the risk of galling, *e.g.* using mating surfaces with similar chemical compositions and mechanical properties, working at elevated temperature or using high load across interface [12]. Stacking fault energy (SFE) is one of the key parameters controlling galling resistance [12,13]. The material having a high amount of stacking fault energy are usually more vulnerable towards galling [14].

However, the influence of microstructure on galling resistance is still unclear. In the literature, most of the work on the influence of microstructure on galling resistant is related to either particle studies (carbides, nitrides…) or crystallographic phases. The effects of the size, spatial distribution and hardness of carbides have been studied in several types of steels [8,15–17]. Homogeneous distribution of small size particles is believed to increase galling resistance while bigger and inhomogeneously distributed particles lower galling resistance. The influence of crystallographic phase on galling resistance has also been studied, in particular in cobalt-base alloys or hard-facing alloys [18,19]. Most of the studies indicates that the galling tendency is increased for phases having c/a ratio low *e.g.* cubic phases. Conversely, HCP structure having an important c/a ratio are less prone to galling [14]. However, these studies on the impact of microstructure on galling resistance are still seldom and it remains hard to have an overall view.

Moreover, one can notice that galling resistance is most often only defined by galling threshold [20]. Even if some authors [21–23] have recently been trying to take galling severity into account, very few data is still to be found in the literature. Additional efforts must be provided to fully apprehend galling phenomenon and propose relevant mechanisms. Classical approach using sole surface investigations has proven to be insufficient to propose trustworthy galling mechanisms. The relationship between microstructure and galling resistance is only slightly considered in the literature. This work combines surface observations and microstructure investigations in order to better characterize galled samples and understand galling mechanisms. To do so, this work is supported by a comparative study using various stainless steel grades. The opposition between microstructural responses from identical galling tests has lead us to propose novel galling categories. These categories will provide a better understanding of the mechanisms behind galling phenomenon and eventually help preventing galling onset.

# 2. Materials and methods

Five stainless steels are selected in this study, namely 316L, 316LN, Nitronic60, AISI660 (austenitic stainless steels) and Uranus45N (duplex austenite-ferrite). These grades differ by their chemical composition, crystallographic structure and mechanical properties, as presented in Table 1 and Table 2. Most data are coming from ThyssenKrupp provider, while surface hardness and grain size are determined experimentally. Surface hardness is determined by nano-indentation using a Berkovich tip with an indentation depth of 1 µm and a peal hold time of 10 seconds. Grains size is measured by Electron BackScatter Diffraction (EBSD) realized on as-received material.

*Table 1 : Chemical composition in mass percent and crystallographic phase of the selected stainless steels*

| | C | Si | Mn | Ni | Cr | Mo | N | Other | Fe (eq) | Phase |
|---|---|---|---|---|---|---|---|---|---|---|
| **Nitronic60** | 0.06 | 4.12 | 8.05 | 8.56 | 17.02 | 0.75 | 0.15 | / | 61.44 | Austenite |
| **AISI660** | 0.08 | 0.34 | 1.30 | 23.35 | 14.5 | 1.16 | / | Ti 2.68 | 56.60 | Austenite PH |
| **Uranus45N** | 0.02 | 0.44 | 1.35 | 5.32 | 22.70 | 2.55 | 0.16 | / | 67.46 | Austenite-ferrite |
| **316L** | 0.02 | 0.58 | 1.30 | 10.08 | 16.90 | 2.03 | 0.04 | / | 69.05 | Austenite |
| **316LN** | 0.01 | 0.29 | 1.85 | 13.25 | 17.05 | 2.61 | 0.16 | / | 64.78 | Austenite |

*Table 2 : Mechanical properties of the selected stainless steels. Surface hardness is determined by nanoindenting tests realized on the surface and grain size is measured by EBSD investigations*

| | $R_e$ (MPa) | $R_m$ (MPa) | $R_m/R_e$ | Elongation (%) | Surface hardness (GPa) | Grain size (µm) |
|---|---|---|---|---|---|---|
| **Nitronic60** | 379 | 732 | 1.93 | 35 | 6.7 ± 1.1 | 126 ± 18 |
| **AISI660** | 635 | 995 | 1.57 | 35 | 8.5 ± 0.9 | 18 ± 7 |
| **Uranus45N** | 542 | 757 | 1.40 | 25 | 7.9 ± 0.7 | 14 ± 6 |
| **316L** | 293 | 555 | 1.89 | 35 | 6.1 ± 1.2 | 34 ± 10 |
| **316LN** | 296 | 626 | 2.11 | 17 | 6.6 ± 0.6 | 75 ± 15 |

Electron BackScatter Diffraction (EBSD) investigations are performed on as-received materials as well as galled samples. Sample preparation for EBSD analysis is done by manual polishing (grid papers up to 4000), followed by 3 µm and 1 µm diamond paste polishing. Finally, vibration polishing is used with 50% OPS – 50% $H_2O$ solution for 10 hours at 100% vibration and 72 hours at 10% vibration. Resulting EBSD orientation maps are presented in Figure 1.

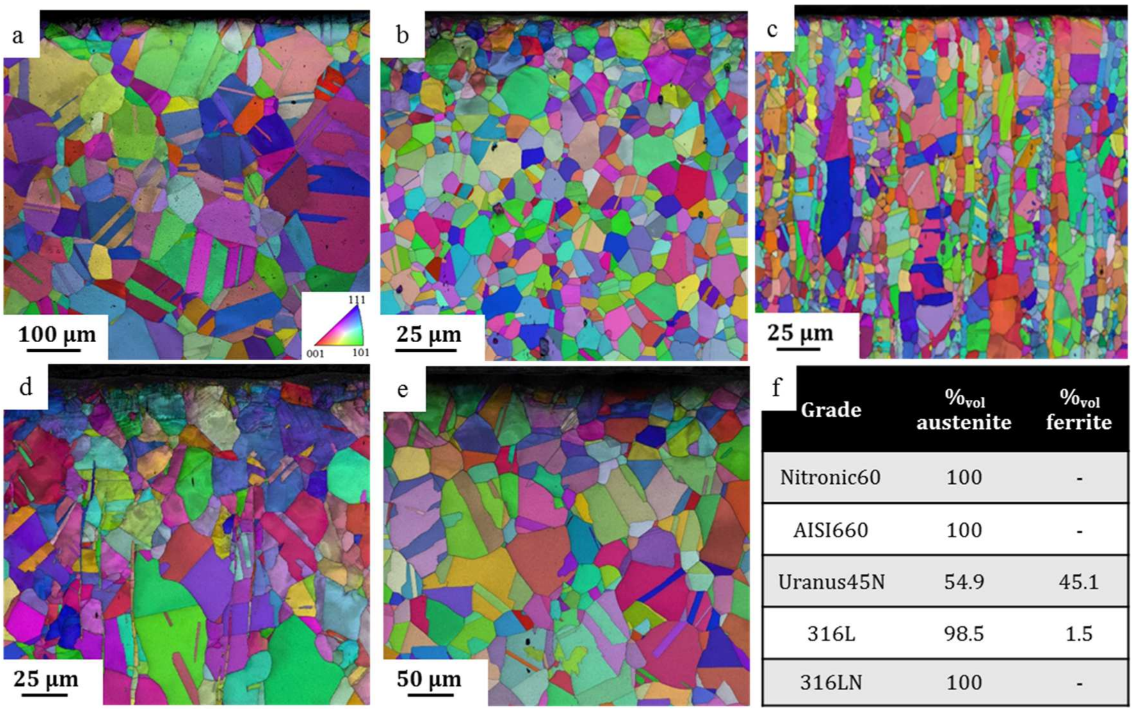


| Grade | $\%_{vol}$ austenite | $\%_{vol}$ ferrite |
|---|---|---|
| Nitronic60 | 100 | - |
| AISI660 | 100 | - |
| Uranus45N | 54.9 | 45.1 |
| 316L | 98.5 | 1.5 |
| 316LN | 100 | - |

*Figure 1: Inverse pole figure (IPF) for the as-received materials. a- Nitronic60, b- AISI660, c- Uranus45N, d- 316L, e- 316LN and f- Austenite and ferrite percent for each grade*

Galling tests are performed following the ASTM G98 standard. It consists of a pin-on-bloc test where a Ø12.7 mm pin rotates on a flat surface. The mating block is always made of 316L since this grade is one of the most used stainless steel in nuclear and pharmaceutical industries. Pins and blocks are directly machined from extruded bars as designed in ASTM G98 standard [2]. All samples come from round bars which have been hot rolled and annealed peeled by the steel providers. All pins are then machined from as received bars in such a way that contact surface is following extrusion direction perpendicular to contact surface. As opposite, due to the important length of tested blocs, contact surface is set parallel to extrusion direction of the initial bar.

Figure 2.a shows the typical pins and plates morphology after galling test, while Figure 2.b represents the cylindrical coordinates system used.

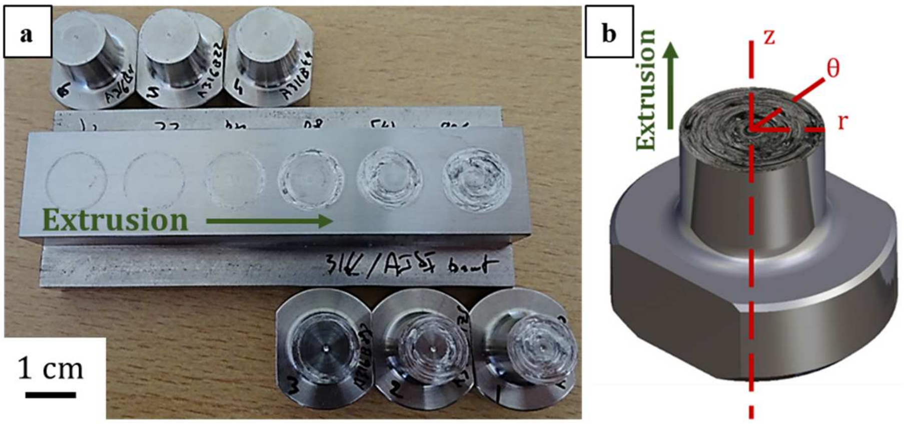


*Figure 2 : a- Pin and block samples after galling tests and b- cylindrical coordinates used for the pin*

Since roughness and surface state are of great importance on galling resistance [4], initial Ra is carefully controlled before galling test. Pins surface are turned while blocks are grinded, with an initial Ra for both pins and plates of 0.30 ± 0.04 µm.

To realize the galling test itself, a tension compression Instron machine (capacity 250kN) is used with a load cell A212-201 (250 kN) [2]. The pin is first subjected to a compressive force, ranging from 8kN to 250kN depending on test condition. The pin is then slowly rotated (one turn in six seconds) while maintaining the contact with the plate (Figure 3.a). One single rotation (360°) is done and the occurrence or not of galling is determined by unassisted visual observation. Galling occurrence is stated if any surface degradation is visible by this sole mean [2]. Each pin is used only once, while blocs can be used for 6 consecutive galling tests, using every time a virgin surface. Galling threshold is determined following a dichotomy tree, starting at a maximum pressure of 350 MPa and then decreased progressively, following the path defined in Figure 3.b. Galling threshold is defined as the average between maximum pressure without galling occurrence and minimum pressure with galling occurrence.

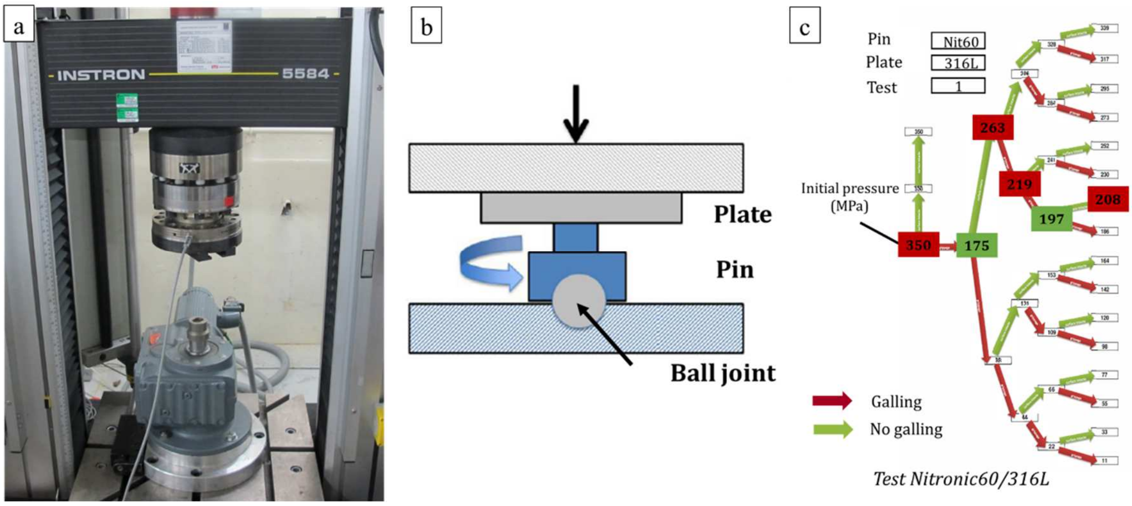


*Figure 3 : a- ASTM G98 experimental galling test setup, b- schematic of the set up used for ASTM G98 galling test and c- ASTM G98 galling test procedure taking as example a Nitronic60/316L test*

After galling test, the occurrence of galling is determined using ASTM G98 8.9 standard. This standard indicates that a sample is galled if any macroscopic surface modification apart from scoring and surface waviness is to be seen with unassisted visual observation. *In situ* acoustic emission measurements could confirm the occurrence of galling, as proposed in Saidoun *et al.* [24].

Surface topography measurement are performed by non-contact 3D profilometry Sensofar S Neox. Material transfer associated with galling is confirmed by Energy-Dispersive Spectroscopy (EDS) on both surfaces. Microscale observations are realized by Scanning Electron Microscopy (SEM) observation on Zeiss Σigma microscope, a current of 25kV is used for both imaging and EBSD mapping. The EBSD patterns acquisition are made with the software Nordif UF1100 and the corresponding mapping done by OIM Data collection 5.3. Local misorientation is determined via Kernel Average Misorientation (KAM) maps. Analyses are either realized following cross section observations (rz section Figure 2.b) or longitudinal observations (rθ section).

# 3. Galling categories investigations

Figure 4 displays the galling thresholds of each considered stainless steel grade tested against a 316L plate. Each test has been repeated three times for repeatability estimations.

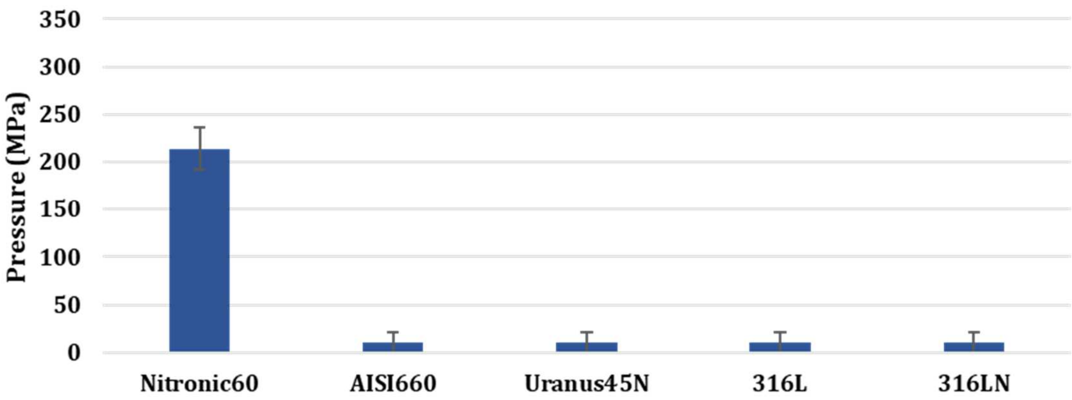


*Figure 4 : Galling threshold in ASTM G98 configuration for different grades of pins mated with a block of 316L*

Selected stainless steels exhibit very low galling threshold, lower than 11 MPa (minimum pressure applicable for this test) except for Nitronic60, having a galling threshold of 214 ± 16 MPa. Considering only galling threshold, one could therefore consider that Nitronic60 presents a high "galling resistance" while the other four grades all present an equivalent galling resistance. However, as presented onwards, galling threshold is not sufficient to determine the galling resistance and noticeable differences can be observed between these five grades.

## 3.1. Surface state investigations

Visual and SEM observations indicate that surface morphology differs from one material to another, as shown on Figure 5.

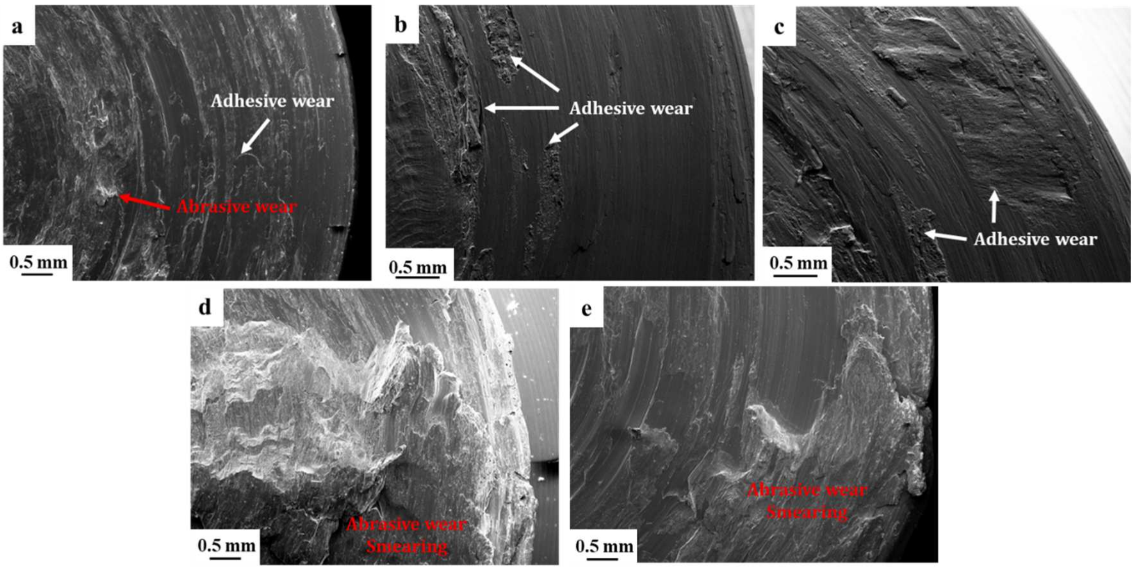


*Figure 5 : SEM observations at mesoscopic scale for samples after galling test at 350 MPa in the case of a- Nitronic60, b- AISI660, c- Uranus45N, d- 316L, e- 316LN*

We observe after galling test at 350 MPa for Nitronic60 a combination of abrasive and adhesive wear of small dimension, leading to a qualitatively weakly degraded surface. AISI660 and Uranus45N exhibit mainly adhesive wear on the surface with the existence of material transfer, confirmed by EDS analysis. Finally, both 316L and 316LN present abrasive wear and smearing observed on the whole surface.

Nitronic60, AISI660 and 316L are the most representative grades for each wear phenomena and are therefore presented in more details. Figure 6 represents typical surfaces observed after galling test at contact pressure slightly higher than galling threshold.

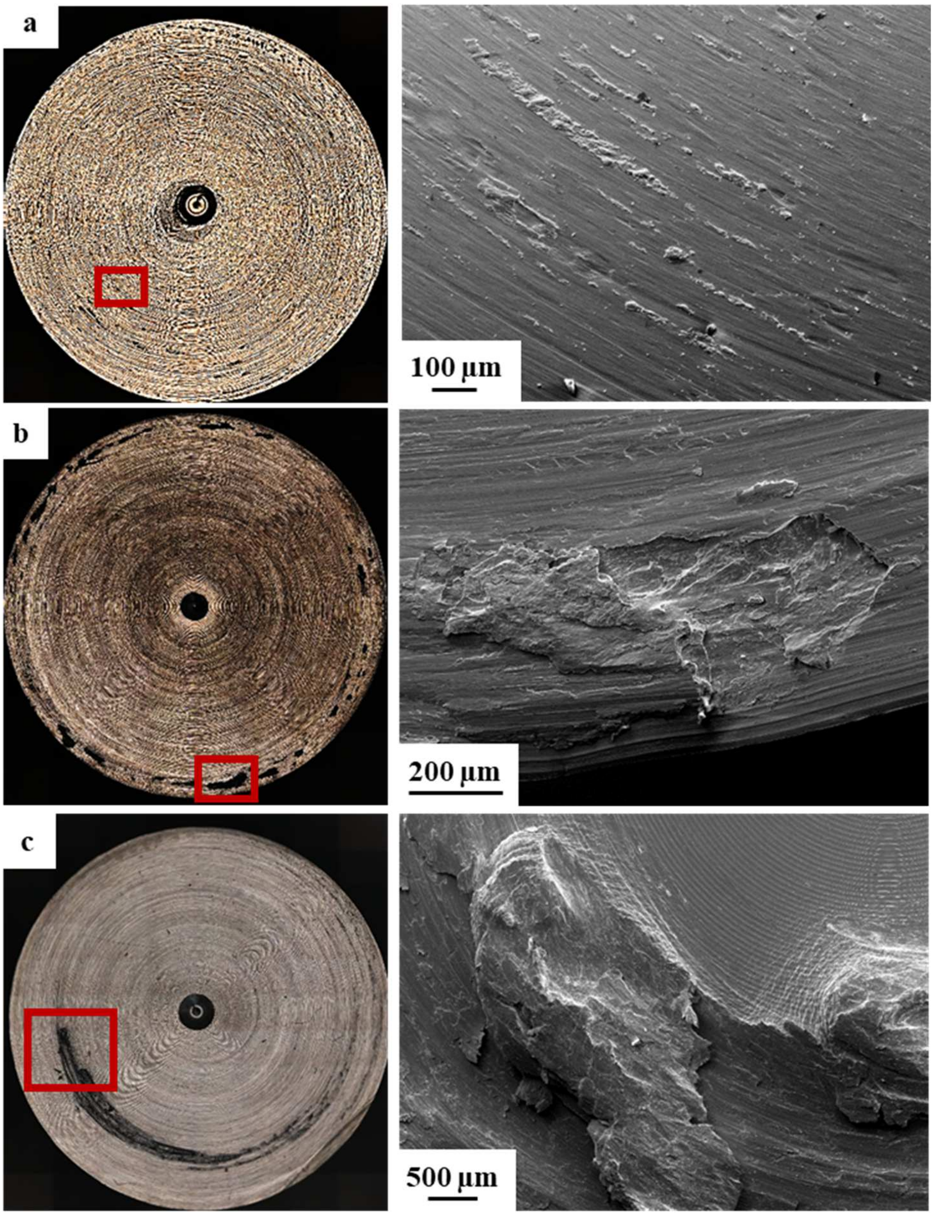


*Figure 6 : Macroscopic observation and SEM observations of the surface slightly higher than galling threshold for a- Nitronic60 at 224 MPa showing localized adhesive wear spots leading to galling initiation sites, b- AISI660 at 22 MPa showing adhesive wear observed along the periphery of the pin and c- 316L at 22 MPa showing third body abrasive wear by smearing observed all over the surface*

Macroscopic observations show that Nitronic60 (Figure 6.a) presents a high number of localized adhesive wear spots homogenously distributed on the whole surface. Material transfer locally occurs at these points, as confirmed by EDS analysis. Almost no smearing or abrasive wear is observed at a pressure slightly higher than galling threshold. In the case of AISI660 (Figure 6.b) wear is mostly adhesive and localized on the periphery of the pin. Almost no wear is observed outside the periphery of the pins. Very little abrasive wear can be found for this grade. Ultimately, 316L (Figure 6.c) shows a high amount of third body abrasive wear and smearing, even at low pressure. Smearing can be found randomly on the whole surface of the pin, especially at higher pressure. Conversely to Nitronic60 and AISI660, adhesive wear is not likely to be found.

These qualitative observations are completed with surface topography investigation (Figure 7). Sa parameter is determined after a galling test realized at 350 MPa. In order to ensure comparative data, measured Sa is then divided by the pressure difference ΔP between 350 MPa and galling threshold (ΔP = 339 MPa for all grades except for Nitronic60: ΔP =136 MPa). Sa value accounts for the consequences of galling test for a given load while the reduced Sa/ΔP is representative of the consequences of galling for a given over-pressure subsequent to galling threshold.

Measurements are realized on a quarter of the surface of the plate (7.5 x 6.5 mm²) to ensure representative data.

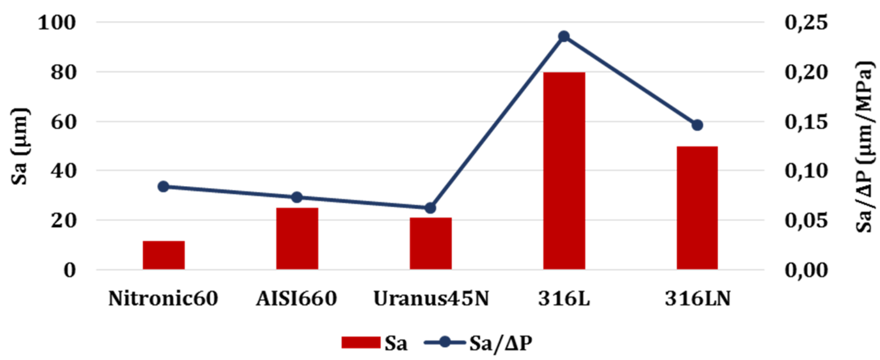


*Figure 7 : Sa parameter measured after galling test realized at 350 MPa. Sa value is then divided by pressure difference in order to have comparative values for different galling thresholds*

Both 316L and 316LN present after galling test at 350 MPa very high Sa values. As opposite, Nitronic60 shows the lowest Sa, while AISI660's and Uranus45N's are intermediary. This is in good agreement with visual inspection and therefore shows that surface degradation due to galling is the most severe for 316L and 316LN. However, when comparing Sa/ΔP, one can notice comparable values between Nitronic60, AISI660 and Uranus45N, meaning that galling severity is equivalent for these grades for a given pressure difference ΔP.

In conclusion, three different wear phenomena, coming with variable galling resistances are observed. These observations suggest the existence of several galling features. In order to confirm this trend, microstructural investigations are performed on galled samples.

### 3.2. Microstructure investigations

EBSD analyses are performed on cross section of galled samples after a test realized at 350 MPa in order to characterize microstructure evolution (Figure 8).

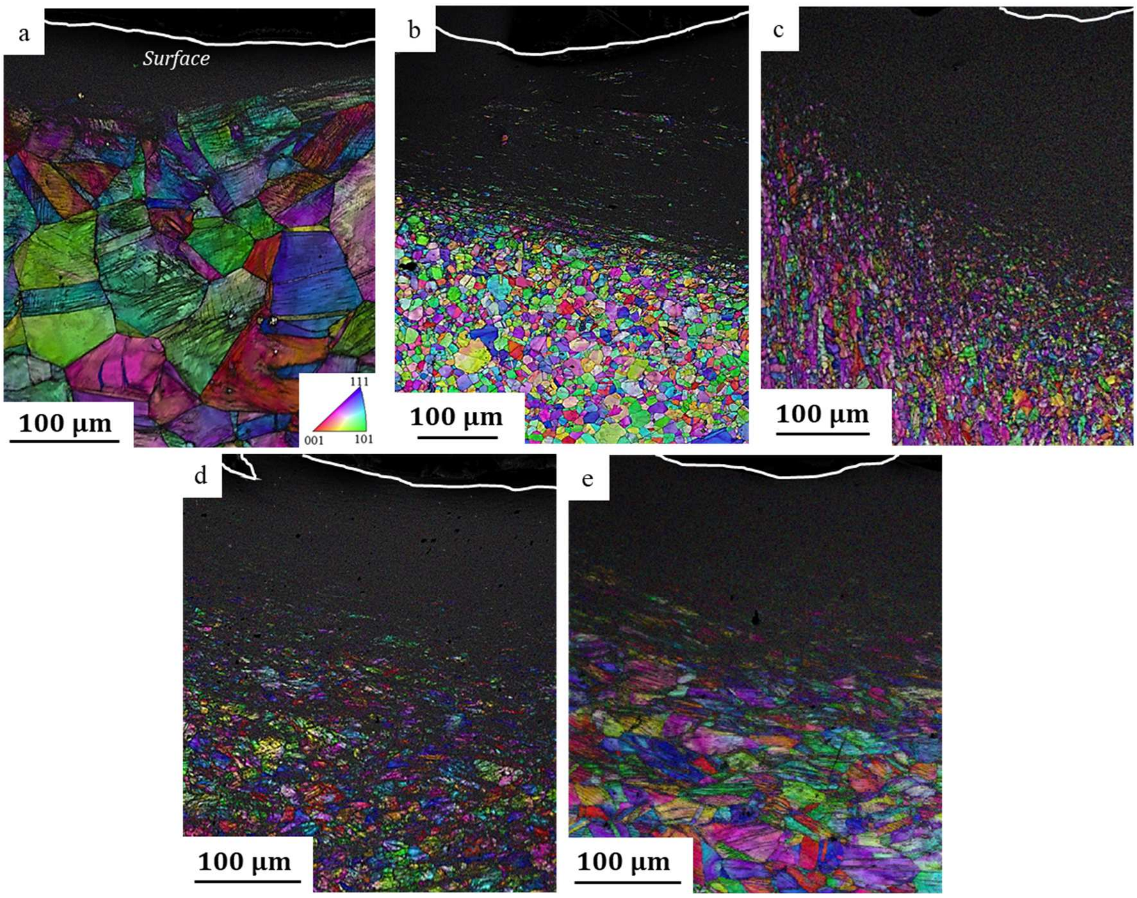


*Figure 8 : Cross section inverse pole figure (IPF) following [RD] for tested pins after galling test realized at 350 MPa. White lines represent the contact surface. a- Nitronic60, b- AISI660, c- Uranus45N, d- 316L, e- 316LN*

For all grades, a non-indexed region is observed in close surface due to the lattice distortion induced during solicitation. However, microstructure evolution differs from one grade to another. The microstructure of Nitronic60 is the least modified by galling apparition while 316L and 316LN show the most deformed microstructure. AISI660, Uranus45N qualitatively present intermediary microstructural degradation.

In order to quantify microstructure changes observed, local misorientation are measured, as proposed in several papers [6,7]. After galling occurrence, local intragranular misorientation rises close to the surface (Figure 9).

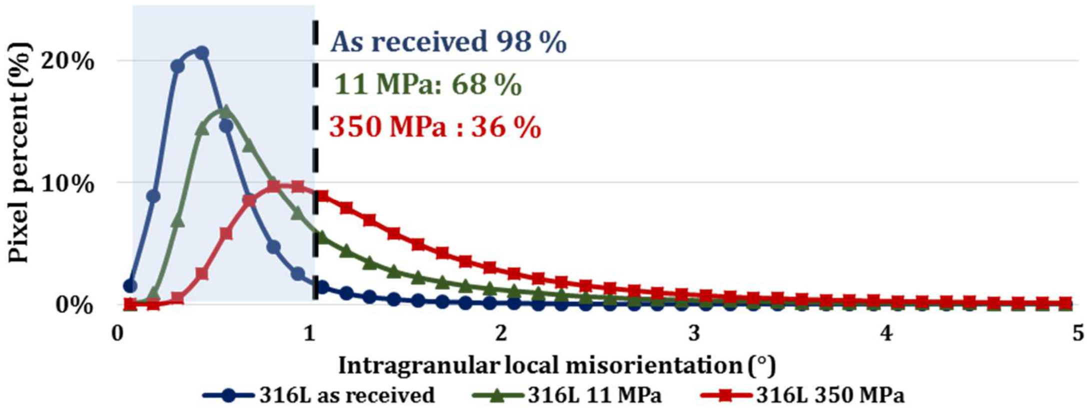


*Figure 9 : Relative frequency associated with a given local misorientation in the case of 316L as received, after a galling test at 11 MPa and after a galling test at 350 MPa*

As seen on Figure 9, at least 96% of the pixel present an intragranular local misorientation lower than 1° before galling test. Once galling occurred, the percentage of pixel having a misorientation lower than 1° rapidly falls to 70% to 30% depending on applied pressure. It is therefore considered that most local misorientation higher than 1° is a result of galling test. Using this information, one can measure the average intragranular misorientation at a given depth and determine the depth until which the microstructure is significantly modified by galling.

Several affected zones are proposed in order to better describe microstructure evolution after galling test (Figure 10).

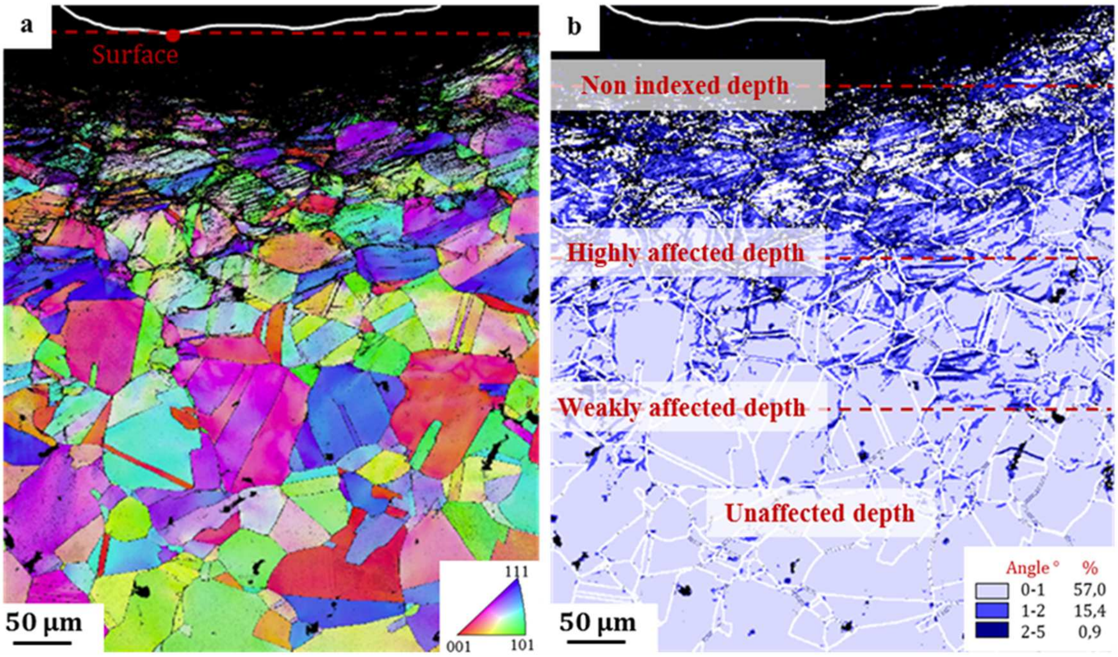


*Figure 10 : a- Inverse pole figure (IPF) of 316L after galling test at 88 MPa and b- corresponding Kernel Average Misorientation (KAM) indicating the local intragranular misorientation*

As shown on Figure 10, four zones are used in this work. So-called “non-indexed depth” corresponds to the depth until more than 70% of pixels can not be indexed by EBSD analysis. Below this zone, the local misorientation is high, with a “strongly affected depth” indicating that at least 70% of pixels are either non-indexed or having an intragranular misorientation higher than 1°. This is followed by a “weakly affected depth” noted *d*, where 30% to 80% of pixels have an intragranular misorientation lower than 1°. Finally, the “unaffected depth” corresponds to the depth from which microstructure is barely affected by galling apparition, with more than 80% of pixels having a local intragranular misorientation lower than 1°. Figure 11 sums up the different affected depths *d* for each considered grade as well as *d*/ΔP.

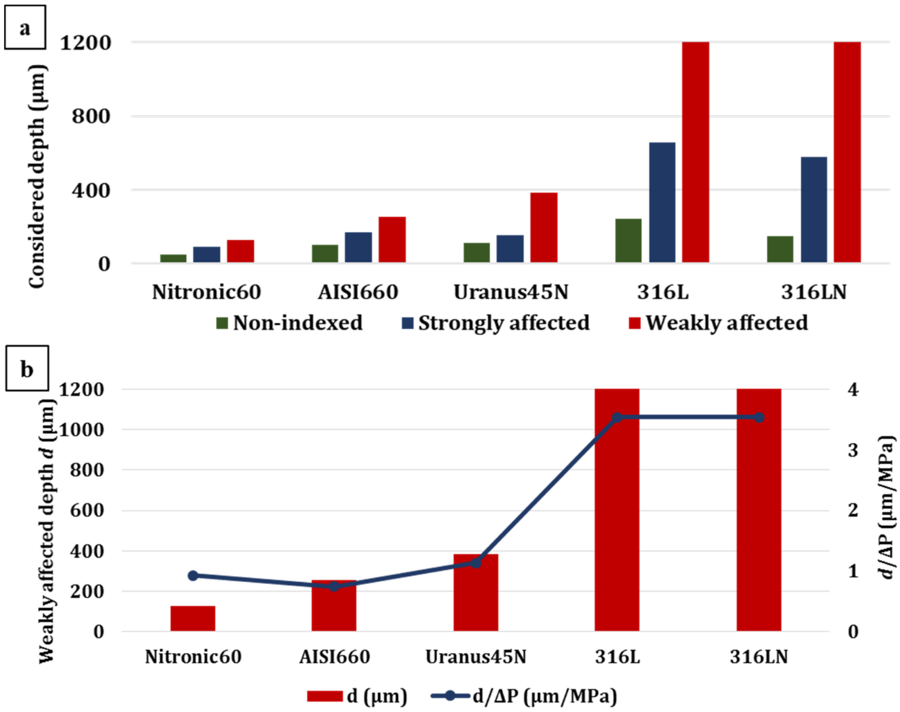


*Figure 11: Determination of a- non-indexed depth, strongly affected depth and weakly affected depth d after galling test realized at 350 MPa for each grade. b- weakly affected depth* d *compared to* d/*ΔP*

Nitronic60 presents both the lowest non-indexed depth, strongly affected depth and weakly affected depth. As opposite, 316L and 316LN both show huge affected depths, with a weakly affected depth higher than 1200 µm, which is the maximum depth investigated. AISI660 and Uranus45N exhibit intermediary values. Once again, when comparing reduced depths, one can notice that Nitronic60, AISI660 and Uranus45N all present equivalent reduced $d/\Delta P$ values. These observations are in good agreement with surface investigations previously discussed.

### 3.3. Identified galling categories

We can conclude from previous investigations that Nitronic60 presents both the lowest surface modification and the slightest microstructural modification, coming with unique wear mechanism. AISI660 and Uranus45 are mainly worn by adhesive wear, leading to a relatively weak surface and microstructure modifications. Finally, 316L and 316LN show similar tendencies, with a mainly abrasive wear and important surface and microstructure modifications. Consequently, three galling categories are proposed herein.

- **Tolerant galling** (Nitronic60) can be described as the category having the highest galling resistance. Galling threshold is high and galling severity is low. Galled samples exhibit a surface state presenting tiny adhesive wear spots, located homogeneously on the pin surface. The in-depth microstructure is also weakly affected.
- **Moderate galling** (AISI660 and Uranus45N) presents mainly adhesive wear, initiated at first at the periphery of the pin. Galling threshold is low but galling severity is low as well. Very few abrasive wear is observed. Both Sa/ΔP and *d*/ΔP of same order of magnitude as for Nitronic60.
- **Severe galling** (316L, 316LN) is the most destructive category and characterized by abrasive wear by third body generation and smearing appearing even at low pressure. Sample surface are heavily deformed, and microstructure is affected for the most important depth. Galling threshold is low and galling severity is high.

# 4. Discussion on galling categories origins

In order to have insights into the origins of these galling categories, several microstructural investigations have been performed. Two main points stands out of these investigations: phase transformation and nanostructuration in close surface.

## 4.1. Phase transformations

Austenite is metastable and subject to phase transformation when applied thermal or mechanical solicitation. In our test configuration, thermal aspects are neglected due to the localization of heat input in extreme surface. However, depending on the Stacking Fault Energy (SFE), the strain applied onto the samples might transform austenite into Strain Induced Martensite (SIM).

SFE is the energy possessed by a structure due to the discontinuity in the stacking planes or closed-pack plane leading to partial dislocations in FCC [14]. SFE strongly affects deformation mechanisms as well as phase transformation during solicitation of a given material [12,25,26].

For low SFE values, typically SFE ≤ 20 $mJ.m^{-2}$ [27], phase transformation is likely to happen. This transformation can lead to either α' martensite (pseudo-cubic body centered) or ε martensite (hexagonal compact) [27,28]. Two transformation sequences are commonly found in the literature: $\gamma \rightarrow \varepsilon \rightarrow \alpha'$ and $\gamma \rightarrow \alpha'$ [29,30]. In the first sequence, ε can act as nucleation sites for the formation of α' while in the second one α' directly forms from austenite γ. However, if only a small amount of strain is provided to the system, the first transformation sequence is stopped and no α' martensite is observed. Thus, depending on the chemical composition and strain history, both α' and ε martensite can be observed. Several strain responses can result from the competition between these phases [31–33] and galling tendency is susceptible to be affected [34].

SFE can be calculated using various methods, including *ab initio* approach [35,36], thermodynamic modelling [37,38], experimental measurements [29,39,40] or approximate models for SFE estimations [41,42]. In this study, the objective is to estimate SFE in order to determine if phase transformation is likely to occur or not. Thus, approximate models are selected instead of more accurate but more complex methodologies. Meric de Bellefon *et al.* [26] (equation 1) proposed one of the most convincing model for austenitic steels, with a good agreement with experimental results, leading to Figure 12 for selected grades.

$$SFE\ (mJ.m^{-2}) = 2.2 + 40*\%_{C} - 3.6*\%_{N} - 0.016*\%_{Cr} + 1.9*\%_{Ni} - 2.9*\%_{Si} + 0.5*\%_{Mn} + 0.77*\%_{Mo} \quad (1)$$

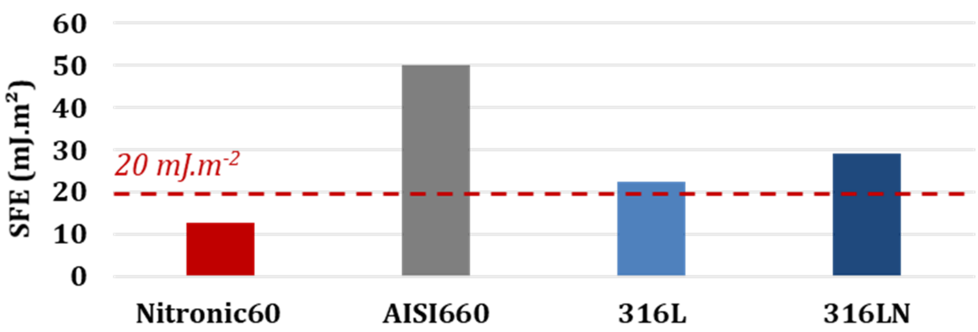


*Figure 12 : Estimated SFE for austenitic stainless steels using Meric de Bellefon* et al. *equation. The dashed line 20 mJ.m$^{-2}$ correspond to the value where phase transformation is likely to be found*

Following this equation, Nitronic60 is the most susceptible to form SIM, while AISI660 is not assumed to present any phase transformation.

Rogers *et al* [43] showed that austenite transforms into an α' pseudo-cubic martensite for galled samples of 316L stainless steel. However, no data could be found in the literature concerning the martensite transformation of other stainless steel grades during galling test.

In order to study the transformed phases, EBSD analyses are performed on galled samples of each austenitic grades. From now on, results are shown for one grade of each galling category: Nitronic60 (tolerant galling), AISI660 (moderate galling) and 316L (severe galling), which present the most representative case.

For Nitronic60 (Figure 13.a), ε martensite is visible in thin laths. No evidence of α' martensite has been found for this grade. As opposite, α' martensite is observed with a pseudo-spherical shape for 316L (Figure 13.b) while no ε martensite could be found. No martensitic transformation has been observed for AISI660 using EBSD analysis.

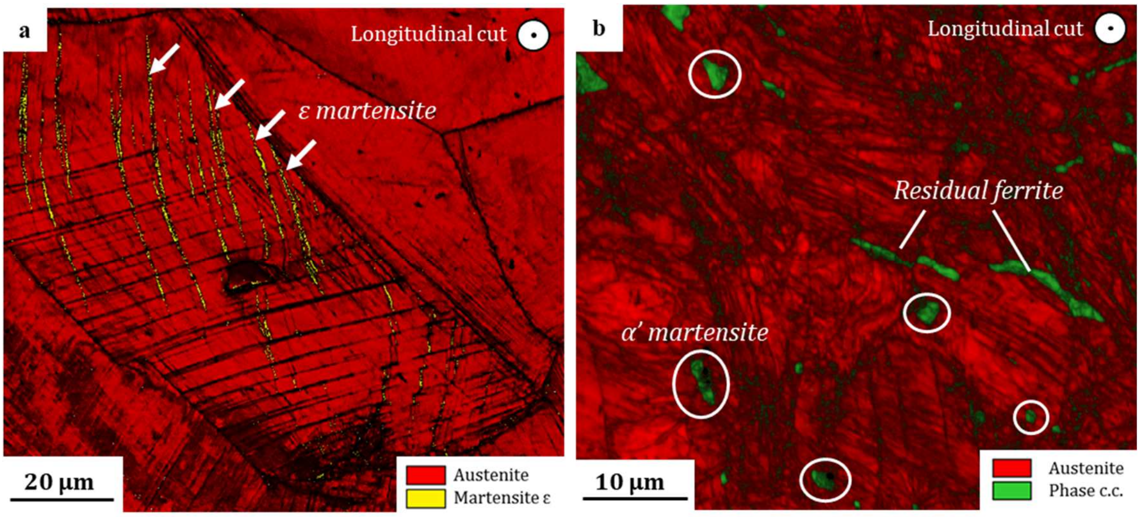


*Figure 13 : Formation after a galling test realized at 350 µm of a- ε martensite inside Nitronic60 (400 µm depth) and b- pseudo-cubic α' martensite inside 316L (550 µm depth)*

It can be concluded that for Nitronic60 (tolerant galling), austenite is transformed into hexagonal compact martensite, while 316L and 316LN (severe galling) form pseudo-cubic body centered martensite. AISI660 (moderate galling) does not show any evidence of phase transformation at this scale.

ε hexagonal compact martensite is most probably beneficial to galling resistance while α' pseudo-cubic body centered martensite might be detrimental [34]. Even if the mechanisms are still unclear, one explanation would be to consider the low number of slip systems in hexagonal compact phase compared to those of body centered phase. Lowering the ease of cross-slip hinders plastic strain diffusion and therefore lowers galling severity [12,44,45]. Therefore, lowering the amount of slip systems for a given configuration could be a way to limit cross-slip and improve galling resistance. Furthermore, the elongated shape of ε martensite as compared to the almost spherical α' makes it more prone to hinder dislocation motion, thus confining dislocations in close surface.

### 4.2. TEM investigations

Finally, TEM investigations have been performed in order to examine the evolution of microstructure in close surface after a galling test realized at 350 MPa.

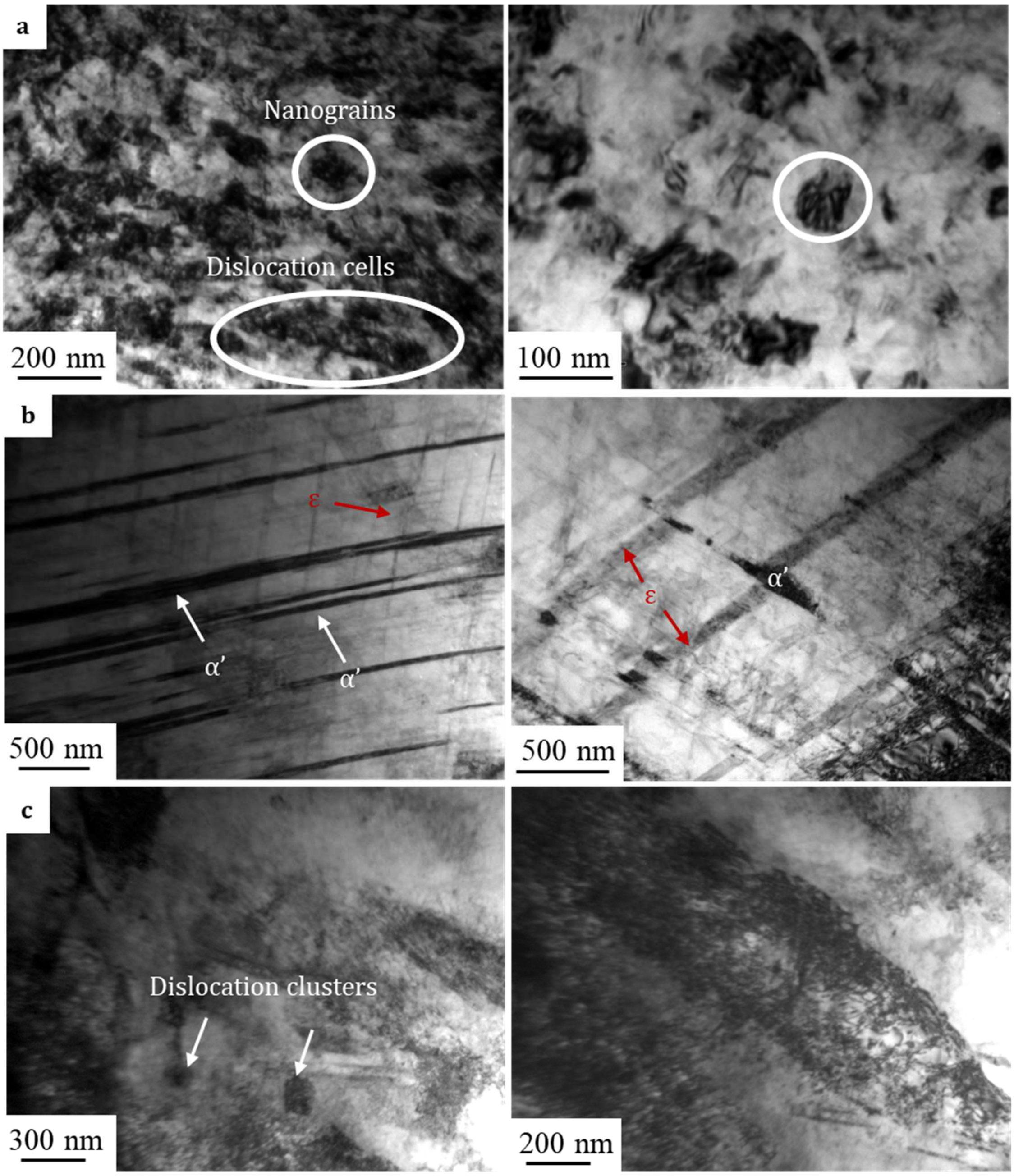


*Figure 14 : TEM investigations realized in extreme surface at one of the sample's valley after a galling test realized at 350 MPa. a- Formation of dislocations cells and nanograins for Nitronic60, b- Martensite laths consisting of mainly α' martensite and a few ε laths in AISI660 c- Statistically distributed dislocations and dislocation clusters in 316L*

Figure 14 shows three distinct microstructures in extreme surface depending on galling category. For Nitronic60, dislocation cells and nanograins of size ranging from 30 nm to 50 nm are observed. This indicates a high capacity of microstructural reorganization for this grade. Moreover, the low depth of affected microstructure pointed out earlier could be explained by the localization of dislocations inside these nanograins. For AISI660, thin laths of both α' martensite and ε martensite are observed. These films could not be observed by EBSD investigation, which suggests that this SIM is only localized at the extreme surface of the sample. The coexistence in extreme surface of both α' and ε martensite reinforces the conclusions drawn in part 4.1 and suggests that the intermediary galling resistance of this grade could originate in this dual phase transformation. For 316L, no microstructural reorganization is found, with statistically distributed dislocations and a few dislocation clusters around the sample. Dislocations are therefore free to migrate to the core material, which may explain the higher affected depth for this grade.

As a result, it is proposed that both ε martensite formation and nanograins formation are beneficial for galling resistance. These differences in phase transformation and microstructure in the extreme surface may explain the differences in galling categories.

# 5. Conclusion

This paper aims at better describing galling phenomena and understanding the consequences of galling apparition. Once galling occurred, several wear mechanisms can be seen depending on selected grade, leading to variable severity of galling. Macroscopic and microscopic investigations (3D profilometry, SEM, EBSD, TEM) performed on five stainless steels allowed us to distinguish three distinct galling mechanisms.

- Tolerant galling appears in the form of adhesive wear spots homogeneously located on sample surface. Both surface degradation and in-depth microstructure evolution the weakest among all the galling categories. Galling threshold is high and galling severity is low.
- Moderate galling presents adhesive wear located solely on pin periphery at low pressure. The weakly affected depth divided by excessive pressure $d/\Delta P$ as well as $Sa/\Delta P$ are of same order as Nitronic60. Both galling threshold and galling severity are low.

- Severe galling is the most destructive type of galling, characterized by a heavily damaged surface, with high amount of third bodies as well as a deeply modified microstructure. Wear is mainly abrasive with an important smearing on the surface. Material transfer, when occurring, is a consequence of third body generation and abrasive wear. Galling threshold is low and galling severity is high.

The origins of the identified galling categories have then been discussed. It appears that for each galling category, different phase transformations can be observed. The transformation from austenite to Strain Induced Martensite (SIM), can be either pseudo-body centered (α') or hexagonal compact (ε). Nitronic60 presents hexagonal compact martensite ε, as opposite to the α' martensite observed in 316L. Moderate galling AISI660 presents both α' and ε martensite in extreme surface. The c/a ratio is higher for ε (hcp) martensite as compared to the quasi-cubic α' martensite, thus, the galling resistance is increased [14].

The formation of nanograins, as seen in Nitronic60 is also suspected to be beneficial to the galling resistance. As opposite, the lack of reorganization in 316L could explain the elevated depth of affected microstructure.

In regards with presented results, the authors recommend to further investigate on the relation between dislocation mobility and galling resistance. Indeed, nanograin formation and hexagonal compact phase transformation, observed for Nitronic60, could be ways to lower the mobility of dislocations and may explain the higher galling resistance of this grade.

## *Acknowledgement*

The authors would like to thank the Hauts-de-France Region and the European Regional Development Fund (ERDF) 2014/2020 for the funding of this work. The authors would also like to thank David CAZE (CETIM Senlis) for galling test realization. Special thanks go to Abdelali OUDRISS and Xavier FEAUGAS from Université de La Rochelle for TEM investigations and exploitation.

## *References*

[1] R. Badji, T. Chauveau, B. Bacroix, Texture, misorientation and mechanical anisotropy in a deformed dual phase stainless steel weld joint, Mater. Sci. Eng. A. 575 (2013) 94–103. https://doi.org/10.1016/j.msea.2013.03.018.

[2] C. Herve, P. Friedrich, Y.-M. Chen, D. Caze, Galling detection by acoustic emission according to ASTM G98, (n.d.).

[3] J. Vikström, Galling resistance of hardfacing alloys replacing Stellite, Wear. 179 (1994) 143–146. https://doi.org/10.1016/0043-1648(94)90232-1.

[4] B. Podgornik, S. Hogmark, Surface modification to improve friction and galling properties of forming tools, J. Mater. Process. Technol. 174 (2006) 334–341. https://doi.org/10.1016/j.jmatprotec.2006.01.016.

[5] P. Karlsson, A. Gåård, P. Krakhmalev, J. Bergström, Galling resistance and wear mechanisms for cold-work tool steels in lubricated sliding against high strength stainless steel sheets, Wear. 286–287 (2012) 92–97. https://doi.org/10.1016/j.wear.2011.04.002.

[6] R. Unnikrishnan, S.M. Northover, H. Jazaeri, P.J. Bouchard, Investigating plastic deformation around a reheat-crack in a 316H austenitic stainless steel weldment by misorientation mapping, Procedia Struct. Integr. 2 (2016) 3501–3507. https://doi.org/10.1016/j.prostr.2016.06.436.

[7] B. Dylewski, M. Risbet, S. Bouvier, The tridimensional gradient of microstructure in worn rails – Experimental characterization of plastic deformation accumulated by RCF, Wear. 392–393 (2017) 50–59. https://doi.org/10.1016/j.wear.2017.09.001.

[8] A. Gåård, P. Krakhmalev, J. Bergström, Influence of tool steel microstructure on origin of galling initiation and wear mechanisms under dry sliding against a carbon steel sheet, Wear. 267 (2009) 387–393. https://doi.org/10.1016/j.wear.2008.11.013.

[9] J. Marteau, Caractérisation multi-échelle et analyse par essai d'indentation instrumentée de matériaux à gradient générés par procédés mécaniques et thermochimiques de traitement de surface, PhD Thesis, Université de Technologie de Compiègne, France, 2013. https://tel.archives-ouvertes.fr/tel-00937956/ (accessed December 21, 2015).

[10] G. Maistro, C. Oikonomou, L. Rogström, L. Nyborg, Y. Cao, Understanding the microstructure-properties relationship of low-temperature carburized austenitic stainless steels through EBSD analysis, Surf. Coat. Technol. 322 (2017) 141–151. https://doi.org/10.1016/j.surfcoat.2017.05.036.

[11] J.P. Hirth, D.A. Rigney, Crystal plasticity and the delamination theory of wear, Wear. 39 (1976) 133–141. https://doi.org/10.1016/0043-1648(76)90229-5.

[12] K.J. Bhansali, A.E. Miller, The role of stacking fault energy on galling and wear behavior, Wear. 75 (1982) 241–252. https://doi.org/10.1016/0043-1648(82)90151-X.

[13] R. Smith, M. Doran, D. Gandy, S. Babu, L. Wu, A.J. Ramirez, P.M. Anderson, Development of a gall-resistant stainless-steel hardfacing alloy, Mater. Des. (n.d.). https://doi.org/10.1016/j.matdes.2018.01.020.

[14] K.K. Kakulite, B. Kandasubramanian, Rudiment of 'galling: Tribological phenomenon' for engineering components in aggregate with the advancement in functioning of the anti-galling coatings, Surf. Interfaces. 17 (2019) 100383. https://doi.org/10.1016/j.surfin.2019.100383.

[15] I. Heikkilä, L. Slycke, Influence of nitrogen alloying on galling properties of pm tool steels, (n.d.).

[16] T. Arai, Y. Tsuchiya, Role of carbide and nitride in antigalling property, Met. Transf. Galling Met. Syst. (1986) 198–216.

[17] D.-C. Ko, S.-G. Kim, B.-M. Kim, Influence of microstructure on galling resistance of cold-work tool steels with different chemical compositions when sliding against ultra-high-strength steel sheets under dry condition, Wear. 338–339 (2015) 362–371. https://doi.org/10.1016/j.wear.2015.07.014.

[18] S.C. Agarwal, H. Ocken, The microstructure and galling wear of a laser-melted cobalt-base hardfacing alloy, Wear. 140 (1990) 223–233. https://doi.org/10.1016/0043-1648(90)90085-O.

[19] H. Ocken, The galling wear resistance of new iron-base hardfacing alloys: a comparison with established cobalt- and nickel-base alloys, Surf. Coat. Technol. (1995) 456–461.

[20] K.C. Anthony, Wear-resistant cobalt-free alloys, J. Mechnical Eng. Technol. 35 (1983) 52–60.
[21] B.M. Voss, M.P. Pereira, B.F. Rolfe, M.C. Doolan, A new methodology for measuring galling wear severity in high strength steels, Wear. 390–391 (2017) 334–345. https://doi.org/10.1016/j.wear.2017.09.002.
[22] S.R. Hummel, Development of a galling resistance test method with a uniform stress distribution, Tribol. Int. 41 (2008) 175–180. https://doi.org/10.1016/j.triboint.2007.07.009.
[23] J.A. Siefert, S.S. Babu, Experimental observations of wear in specimens tested to ASTM G98, Wear. 320 (2014) 111–119. https://doi.org/10.1016/j.wear.2014.08.017.
[24] A. Saidoun, C. Herve, Y.M. Chen, T. Lesage, S. Bouvier, Galling detection by acoustic emission (AE) according to ASTM G98, in: 2018.
[25] D. Arpan, Revisiting stacking fault energy of steels, Metall. Mater. Trans. A. (2015). https://doi.org/10.1007/s11661-015-3266-9.
[26] G. Meric de Bellefon, J.C. van Duysen, K. Sridharan, Composition-dependence of stacking fault energy in austenitic stainless steels through linear regression with random intercepts, J. Nucl. Mater. 492 (2017) 227–230. https://doi.org/10.1016/j.jnucmat.2017.05.037.
[27] O. Grässel, G. Frommeyer, C. Derder, H. Hofmann, Phase Transformations and Mechanical Properties of Fe-Mn-Si-AlTRIP-Steels, J. Phys. IV. 07 (1997) C5-383-C5-388. https://doi.org/10.1051/jp4:1997560.
[28] A. Saeed-Akbari, J. Imlau, U. Prahl, W. Bleck, Derivation and Variation in Composition-Dependent Stacking Fault Energy Maps Based on Subregular Solution Model in High-Manganese Steels, Metall. Mater. Trans. A. 40 (2009) 3076–3090. https://doi.org/10.1007/s11661-009-0050-8.
[29] D.T. Pierce, J.A. Jiménez, J. Bentley, D. Raabe, J.E. Wittig, The influence of stacking fault energy on the microstructural and strain-hardening evolution of Fe–Mn–Al–Si steels during tensile deformation, Acta Mater. 100 (2015) 178–190. https://doi.org/10.1016/j.actamat.2015.08.030.
[30] Y. Li, W. Li, N. Min, W. Liu, C. Zhang, X. Jin, Mechanical response of a medium manganese steel with encapsulated austenite, Scr. Mater. 178 (2020) 211–217. https://doi.org/10.1016/j.scriptamat.2019.11.033.
[31] K. Spencer, M. Véron, K. Yu-Zhang, J.D. Embury, The strain induced martensite transformation in austenitic stainless steels: Part 1 – Influence of temperature and strain history, Mater. Sci. Technol. 25 (2009) 7–17. https://doi.org/10.1179/174328408X293603.
[32] Q.X. Dai, X.N. Cheng, X.M. Luo, Y.T. Zhao, Structural parameters of the martensite transformation for austenitic steels, Mater. Charact. 49 (2002) 367–371. https://doi.org/10.1016/S1044-5803(03)00035-4.
[33] W. Pachla, J. Skiba, M. Kulczyk, S. Przybysz, M. Przybysz, M. Wróblewska, R. Diduszko, R. Stępniak, J. Bajorek, M. Radomski, W. Fąfara, Nanostructurization of 316L type austenitic stainless steels by hydrostatic extrusion, Mater. Sci. Eng. A. 615 (2014) 116–127. https://doi.org/10.1016/j.msea.2014.07.069.
[34] K.-L. Hsu, T.M. Ahn, D.A. Rigney, Friction, wear and microstructure of unlubricated austenitic stainless steels, Wear. 60 (1980) 13–37. https://doi.org/10.1016/0043-1648(80)90247-1.
[35] T.L. Achmad, W. Fu, H. Chen, C. Zhang, Z.-G. Yang, First-principles calculations of generalized-stacking-fault-energy of Co-based alloys, Comput. Mater. Sci. 121 (2016) 86–96. https://doi.org/10.1016/j.commatsci.2016.04.031.
[36] K.R. Limmer, J.E. Medvedeva, D.C.V. Aken, N.I. Medvedeva, Ab initio simulation of alloying effect on stacking fault energy in fcc Fe, Comput. Mater. Sci. 99 (2015) 253–255. https://doi.org/10.1016/j.commatsci.2014.12.015.
[37] S. Curtze, V.-T. Kuokkala, A. Oikari, J. Talonen, H. Hänninen, Thermodynamic modeling of the stacking fault energy of austenitic steels, Acta Mater. 59 (2011) 1068–1076. https://doi.org/10.1016/j.actamat.2010.10.037.

[38] R. Li, S. Lu, D. Kim, S. Schönecker, J. Zhao, S.K. Kwon, L. Vitos, Stacking fault energy of face-centered cubic metals: thermodynamic and ab initio approaches, J. Phys. Condens. Matter. 28 (2016) 395001. https://doi.org/10.1088/0953-8984/28/39/395001.

[39] W. Reick, M. Pohl, A. Padilha, Determination of stacking fault energy of austenite in a duplex stainless steel, Steel Res. 67 (1996) 253–256. https://doi.org/10.1002/srin.199605486.

[40] D.T. Pierce, J.A. Jiménez, J. Bentley, D. Raabe, C. Oskay, J.E. Wittig, The influence of manganese content on the stacking fault and austenite/ε-martensite interfacial energies in Fe–Mn–(Al–Si) steels investigated by experiment and theory, Acta Mater. 68 (2014) 238–253. https://doi.org/10.1016/j.actamat.2014.01.001.

[41] R.E. Schramm, R.P. Reed, Stacking fault energies of seven commercial austenitic stainless steels, Metall. Trans. A. 6 (1975) 1345–1351. https://doi.org/10.1007/BF02641927.

[42] T. Yonezawa, K. Suzuki, S. Ooki, A. Hashimoto, The Effect of Chemical Composition and Heat Treatment Conditions on Stacking Fault Energy for Fe-Cr-Ni Austenitic Stainless Steel, Metall. Mater. Trans. A. 44 (2013) 5884–5896. https://doi.org/10.1007/s11661-013-1943-0.

[43] S.R. Rogers, D. Bowden, R. Unnikrishnan, F. Scenini, M. Preuss, D. Stewart, D. Dini, D. Dye, The interaction of galling and oxidation in 316L stainless steel, Wear. 450–451 (2020) 203234. https://doi.org/10.1016/j.wear.2020.203234.

[44] D.H. Buckley, Surface effects in adhesion, friction, wear, and lubrication, 1981. https://www.elsevier.com/books/surface-effects-in-adhesion-friction-wear-and-lubrication/buckley/978-0-444-41966-8 (accessed August 20, 2018).

[45] D.H. Buckley, The Influence of the Atomic Nature of Crystalline Materials on Friction, E Trans. 11 (1968) 89–100. https://doi.org/10.1080/05698196808972212.